sustainability

MDPI

Article

Investigating Disaster Mechanisms Triggered by Abrupt Overburden Fracture Alterations in Close-Seam Mining Beneath an Exceptionally Thick Sandstone Aquifer

Tao Yan [1], Chuanqu Zhu [1,*], Qingfeng Li [1] and Qian Xu [2]

[1] School of Resource & Environment and Safety Engineering, Hunan University of Science and Technology, Xiangtan 411201, China; yanjiahong168@sina.com (T.Y.); lqfchina@126.com (Q.L.)

[2] School of Safety Science and Engineering, Changzhou University, Changzhou 213164, China; chinaxuqian@126.com

* Correspondence: yantao910524@gmail.com; Tel.: +86-19831602919

Abstract: The influx of roof water from exceptionally thick sandstone aquifers in northwestern China's mining regions presents considerable challenges to the safety and productivity of coal mining operations. However, a significant gap in the literature persists concerning the underlying mechanisms. In this study, we investigated coal-seam mining beneath the exceptionally thick sandstone aquifer of the Zhiluo Formation at the Lingxin Coal Mine, utilizing this context as the basis for our engineering analysis. Our examination probed the hydrogeological and geomechanical mechanisms responsible for the abrupt alterations in overburden fractures and their catastrophic consequences during close-seam mining operations, employing research methodologies such as a theoretical analysis, fluid–structure-coupled simulation, and comparative evaluation. The study highlighted the intricate interplay between compressive-shear loads and the mechanics of hydraulic fracturing processes. The results revealed that in the absence of waterproof coal pillars, the downward mining of the L1614, L1615, and L1616 working faces led to the overlying rock's water-conducting fractures reaching 204.9 m. This height was equivalent to 20 times the combined mining thickness of the three coal seams, impacting both the K3 and K4 aquifers. Conversely, when the water-resistant coal pillars were retained during the downward mining of the L1814, L1815, and L1816 working faces, the maximum height of the water-conducting fractures in the overlying rock was 103.5 m. This height was 10 times the combined mining thickness of the three coal seams, affecting only the K4 aquifer. Notably, vertical hydraulic fracturing was observed when the water pressure variation in the K3 aquifer exceeded 2–3 times its initial value. The water-conducting fracture zone was primarily characterized by the presence of "Type I-II" fractures, with the termination point of each fracture influenced by pressure and shear forces. Furthermore, we established a "fracture cracking and propagation model" and a "hydraulic fracturing-induced disaster model" based on the principles of fracture mechanics. We also provided formulas for calculating the cracking angles and extension heights of overburden fractures' endpoints, which were derived from the maximum normal stress criterion.

Keywords: exceptionally thick sandstone aquifers; close-seam mining; fracture extension; abrupt overburden fracture alterations; hydraulic fracturing

check for updates

Citation: Yan, T.; Zhu, C.; Li, Q.; Xu, Q. Investigating Disaster Mechanisms Triggered by Abrupt Overburden Fracture Alterations in Close-Seam Mining Beneath an Exceptionally Thick Sandstone Aquifer. *Sustainability* **2023**, *15*, 13845. https://doi.org/10.3390/su151813845

Academic Editors: Fan Feng, Eryu Wang and Ruifeng Huang

Received: 10 August 2023
Revised: 12 September 2023
Accepted: 15 September 2023
Published: 18 September 2023

1. Introduction

Given the abundance of coal, scarcity of oil, and limited gas resources in China, coal will continue to hold a primary position in the country's non-renewable energy structure for an extended period [1,2]. As recoverable coal reserves in eastern China are nearing depletion, it is anticipated that the primary coal source will transition to the western region. Here, the extraction primarily involves Jurassic coal seams. These mines have the following unique hydrogeological characteristics: the coal seams are deeply located, closely stratified, and underlain by a significant sandstone aquifer from the Zhiluo Formation [3].

This aquifer is marked by high water pressure, copious water content, and significant permeability. Mining closely situated seams may intensify roof deterioration, reduce the stability duration of surrounding rock pressure, and lead to water-conducting fracture heights that surpass established estimates [4–7]. A primary risk is the thick sandstone aquifer in the overlying strata, which signifies a considerable water source. If fractures penetrate this aquifer, it could result in water inrush at the mining face, potentially causing lost underground equipment, operational interruptions, and, tragically, miner fatalities. Therefore, a thorough investigation into the disaster mechanisms instigated by sudden shifts in overburden fractures during close-seam mining beneath an exceptionally thick sandstone aquifer is crucial.

Extensive research has been conducted on the patterns of overlying rock failure following the extraction of adjacent coal seams. Coal mining operations have typically employed a top-down sequence for sequential coal-seam extraction [8]. This method involves mining the upper seam before shifting the focus to the lower seam. The removal of the upper seam triggers a redistribution of inherent primary stress within the neighboring rock, leading to an increase in stress [9–11]. Consequently, the overlying rock strata, already containing primary fractures, transitions into a state of stress imbalance [12–14]. Should the increased stress exceed the shear strength at the endpoints of the original fractures, these fractures will begin to crack and intersect with nearby fractures. This has resulted in reductions in the load-bearing capacities of adjacent rock masses while encouraging fracture expansion and transferring stress to farther-away rock masses with higher load-bearing potentials [15–17]. This mechanism continues until the stress on the critical layer reaches its maximum, potentially initiating instability and fracturing and resulting in a collapse zone [18]. The mined-out area of an upper coal seam undergoes a dynamic load cycle, transitioning through phases of “unloading-roof cracking-roof collapse-compaction” [19,20]. This mined-out area, along with the remaining coal pillars, contributes to the formation of a fragmented roof in the lower coal seam. The fracturing of the critical layer in the upper seam diminishes its support capacity for the overlying load, leading to direct pressure on the fragmented roof during the extraction of the lower seam. This pressure results in stress concentrations and reductions in the final fracturing spans, leading to the expansion of fractures both higher and farther within the roof [21,22]. This propagation only ceases when the rock mass possesses enough strength to withstand the applied pressure. Other research has scrutinized the dynamics of roof-water inrush after monolithic coal-seam extraction beneath sandstone aquifers. This exploration primarily concerns the representative hydrogeological attributes of mining areas in western China, where sandstone aquifers are commonly positioned above coal-seam roofs [23]. These aquifers exhibit characteristics such as substantial pore sizes, wide pore throat radii, and pronounced porosity, features that promote both the accumulation and transmission of groundwater [24–26]. Post-mining procedures often lead to the formation of a water-conducting fracture zone in the roof, which is characterized by considerable height and marked water conductivity [27–29]. This scenario amplifies the possibility of water inrush from a superimposed sandstone aquifer. When an aquifer’s thickness is insufficient and its water content is relatively low, a pulsatory water influx is observed [30]. On the other hand, if an aquifer exhibits greater thickness and a moderate-to-high water content, a persistent water influx may be anticipated [31]. In situations where an aquifer is exceptionally thick and possesses a high water content, a stratified layer of water influx tends to manifest [32–35]. In summary, current studies have predominantly examined the overlying rock failure patterns and roof water inrush dynamics in isolation. Concerning the former, close-seam mining operations typically use a top-down method, causing stress redistribution in the surrounding rock and potentially initiating instability and fracturing, which impact the safety and efficiency of subsequent lower-seam extractions due to changes in stress patterns and rock mass strengths. Regarding the matter of roof-water inrush dynamics, for sandstone aquifers above coal seams that have properties facilitating groundwater accumulation and transmission, post-mining processes often create water-conductive fracture zones, increasing the risk of water inrush from these aquifers, with the influx nature varying based on the aquifer's thickness and water content. However, few studies in the literature have addressed the anomalous development mechanism of overlying rock fractures from a mechanical standpoint, especially under conditions marked by significant changes in surrounding rock pressures due to the proximity to multi-seam mining and hydraulic fracturing triggered by thick sandstone aquifers overhead [36–40]. This mechanism is the central focus of this paper.

This study aimed to determine the stress distributions, cracking angles, and extension heights of overburden fractures' terminal points. Additionally, the study examined the impact of the presence or absence of waterproof coal pillars at the working face boundary on the development heights of these fractures and the influence of aquifer water pressure magnitude on the likelihood of sudden water inrush events during hydraulic fracturing. The research methodology employed in this study encompassed three primary approaches: a fluid–structure-coupled simulation, which involved the creation of small-scale physical test benches to replicate the hydrogeological conditions of coal mines and the subsequent damage to overlying rock post-mining; a comparative evaluation, which entailed comparing and analyzing the development heights of the overlying rock fractures by installing impermeable coal pillars (not in the uphill and downhill directions of the coal seams), as well as pressurizing the K3 aquifer to assess the water pressure values that could induce hydraulic fracturing in the underlying rock strata; and a theoretical analysis, which applied a fracture mechanics theory to determine the cracking angles and extension heights of the terminal points of the overburden fractures.

2. Materials and Methods

2.1. A Comprehensive Review of the Hydrogeological Conditions at the Lingxin Coal Mine

The Lingxin Coal Mine, located in the Ningdong Coalfield, primarily extracts the #14, #15, and #16 coal seams from the Yan'an Formation of the Middle and Lower Jurassic periods. These coal seams exhibit dip angles of approximately 10°. The average mining thicknesses for the coal seams are 2.8 m, 3.2 m, and 4.3 m, respectively, while the coal-seam spacings are 17.3 m and 11.3 m. Mining has occurred in the upward direction of the working face, with the downward direction pending. The advancing distance for each working face is approximately 180 m. The K3 and K4 aquifers are distributed above the roof of the #14 coal seam. The average thickness of the K3 aquifer is 87.2 m, and its lithology primarily consists of medium sandstone. Pumping tests have indicated a unit water inflow of 1.1–1.8 $L \cdot s^{-1} \cdot m^{-1}$, suggesting a highly water-rich aquifer. The lithology of the K4 aquifer mainly comprises fine sandstone and exhibits a weak water abundance.

The primary mechanical parameters of the coal-bearing strata are presented in Table 1.

Table 1. Primary mechanical parameters of the coal-bearing strata.

Rock Formation Property	Thickness (m)	Compressive Strength (MPa)	Tensile Strength (MPa)	Bulk Density ($kg \cdot m^{-3}$)	Cohesion Strength (MPa)
Medium sandstone	19.00	28.70	0.34	2.43×10^3	1.45
Fine sandstone	9.60	30.10	0.33	2.51×10^3	1.15
Medium sandstone	2.20	27.20	0.25	2.40×10^3	0.90
Fine sandstone	10.40	30.60	0.28	2.51×10^3	1.10
Siltstone	11.30	33.40	0.35	2.66×10^3	1.30
Medium sandstone (K3 aquifer)	87.20	32.50	0.55	2.57×10^3	1.75
Siltstone	11.70	33.40	0.35	2.66×10^3	1.30
Fine sandstone (K4 aquifer)	29.80	29.60	0.39	2.52×10^3	1.20
Siltstone	30.30	37.50	0.38	2.68×10^3	1.55
#14 coal seam	2.80	18.50	0.43	1.40×10^3	1.00
Siltstone	17.30	36.80	0.38	2.64×10^3	1.90
#15 coal seam	3.20	16.60	0.47	1.45×10^3	1.20
Siltstone	11.30	34.00	0.43	2.64×10^3	1.80
#16 coal seam	4.30	13.70	0.54	1.38×10^3	1.00

2.2. Fluid–Structure Coupling Similarity Simulation Experiment

2.2.1. Development of the Formation-Similar Materials

In this study, a two-dimensional fluid–structure coupling similarity simulation experimental platform was used to construct a model, with the dimensions of length × width × height equal to 3.20 m × 0.25 m × 1.00 m, respectively. Considering the platform's size and the mine's hydrogeological data, the model's geometric similarity ratio was established as 1:250, with a unit weight similarity ratio of 1:1.5, a time similarity ratio of 1:16, and an elastic modulus similarity ratio of 1:375. The rock layers were composed of sand, gypsum, calcium carbonate, gravel, and petroleum jelly [41].

(1) Development of the stratum materials

The stratum materials, comprising a proportionate mixture of sand, gypsum, and calcium carbonate, were synthesized as specified in Table 2.

(2) Development of the aquifuge materials

Table 2. Proportions of the stratum materials.

Lithology	Proportions	Lithology	Proportions
Medium sandstone	746	Siltstone	882
Fine sandstone	864	Coal seam	982

The existing water barrier consists of siltstone. A mixture of sand, gypsum, and calcium carbonate was prepared according to the proportions specified in Table 2 before incorporating heated petroleum jelly at 200 °C. By utilizing an optimal combination of petroleum jelly, the water barrier maintained its hydrophobic properties while preserving a certain degree of deformation capacity [42].

(3) Development of the aquifer materials

A rock's permeability depends on its porosity, which is primarily influenced by factors such as particle size, particle distribution, and particle shape [42]. To meet the mechanical property requirements of the aquifer, block stones (particle sizes of >10 mm), pebbles (particle sizes of 2 mm), and coarse sand (particle sizes of <1 mm) were selected and combined in ratios of 3:3:4, 5:3:2, 7:2:1, 8:1:1, and 9:1:0. Compressive strength and permeability tests were performed on the graded rock samples to identify the aggregate ratio that most closely replicated the native aquifer's performance. For the K3 and K4 aquifers, the ratios were as follows: block stone: pebble: coarse sand = 5:3:2, and aggregate (block stone + pebble + coarse sand): gypsum: calcium carbonate = 7:7:3.

2.2.2. The Experimental Process

In the process of constructing the model, eight stress monitoring lines were strategically placed along the coal-seam direction, each outfitted with eight stress sensors. Four water pressure sensors were installed in both the K3 and K4 aquifers. The DH3816N static strain gauge was utilized to monitor real-time fluctuations in overburden stress and aquifer water pressure. Following a one-month natural curing period, a digital speckle grid was applied to the model's boundary, extending from the base of the #16 coal seam to its top (Figure 1). A high-precision digital camera documented the development of the overlying rock fractures, and Match ID software (version 1.0) was employed to record and analyze the alterations in the strain field of the overlying rock after the coal-seam mining.

Taking into account the actual mining conditions, an automatic water injection device introduced water into the aquifer before mining. The coal seam was subsequently extracted using a downward mining method, with the L1614, L1615, and L1616 working faces mined in sequence. After stabilizing the overlying rock during each mining phase, the stress, strain, water pressure, water inflow, and water inrush points of the overburden were observed. Subsequently, the L1814, L1815, and L1816 working faces were mined. Each working face was mined for 120 s.

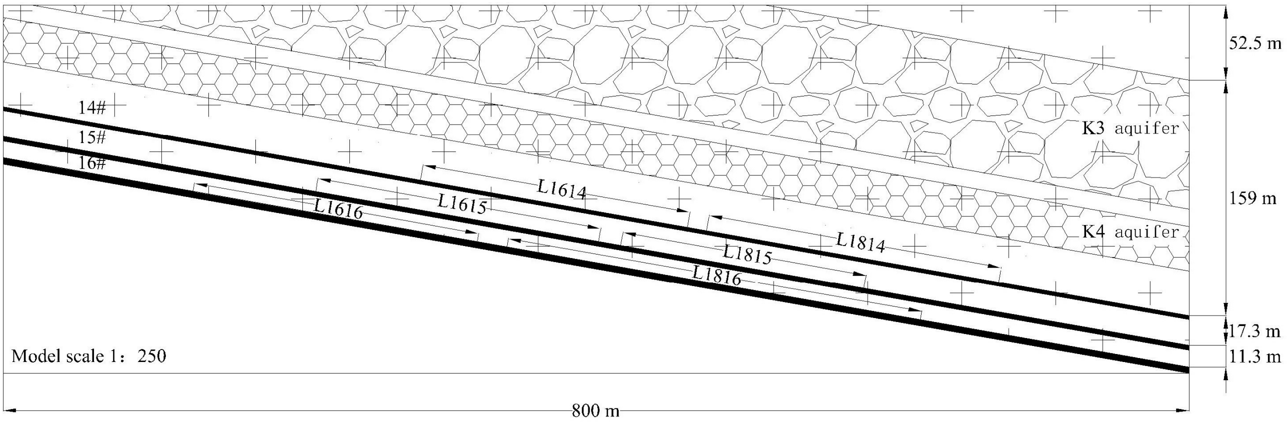

Figure 1. Schematic diagram of a fluid–structure coupling similarity simulation experiment.

3. Results

3.1. Evolutionary Patterns of the Overlying Rock Fractures in the Absence of Water-Resistant Coal Pillars

Following the sequential mining of the L1614, L1615, and L1616 working faces, a map depicting the development of the overlying rock fractures was created, and it is presented in Figure 2. After excavating the L1614 working face, the overlying rock fractures extended to a height of 43 m, reaching the middle of the K4 aquifer, with only three minor water inrush points observed. During the excavation of the L1615 working face, the fractures expanded to a height of 113.7 m, penetrating both the middle and lower sections of the K3 aquifer and resulting in six minor water inrush points. Following the full excavation of the L1616 working face, the fractures extended to a height of 204.9 m, marking an increase of 125.8 m from the L1614 excavation, and eight significant water inrush points were identified in the goaf.

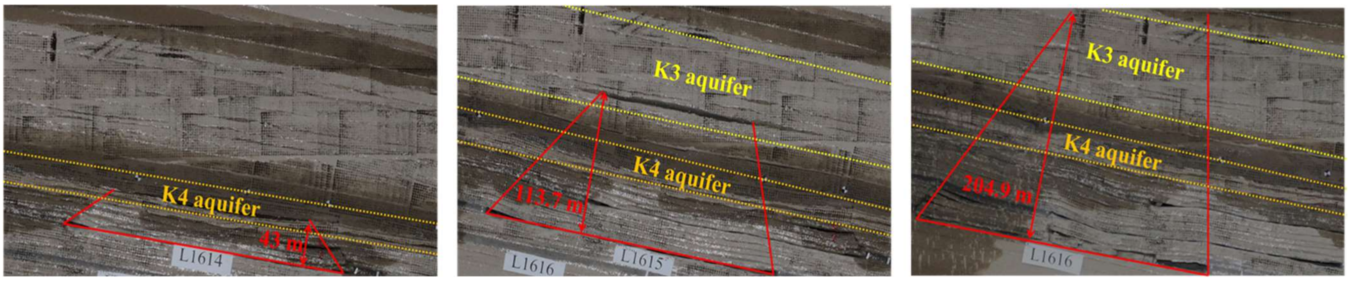

Figure 2. Map illustrating the evolution of the overburden rock fractures in the L1614, L1615, and L1616 working faces post-mining.

As illustrated in Figure 2, the fractures within the collapse zone predominantly consisted of open-type (Type I) fractures while those in the water-conducting fracture zone were mainly composed of "open-slip" composite-type (Type I-II) fractures. A schematic diagram demonstrating the cracking and extension of the overlying rock fractures was developed (Figure 3). By incorporating the primary mechanical parameters of the coal-bearing strata into the Match ID software and analyzing the deformation of the digital speckle grid on the model's surface, along with the changes in the pressure sensor values, the inclination angles and stress conditions of the outermost fracture endpoints B and B_2 above the cessation mining line could be examined. Following the mining of the L1614 working face (time $\approx$ 120 s), the vertical stress at the outermost fracture endpoint B above the cessation line was -1.31 MPa, the horizontal stress was -0.69 MPa, the shear stress was -0.34 MPa, and the fracture inclination angle was 55°. As a result, endpoint B experienced a significant compressive–shear load. After mining the L1615 and L1616 working faces (time ≈ 360 s), the vertical stress at the outermost fracture endpoint B_2 above the cessation line was −0.65 MPa, the horizontal stress was −0.54 MPa, the shear stress was −0.24 MPa, and the fracture inclination angle was 65°. Consequently, endpoint B_2 was also subjected to a compressive–shear load.

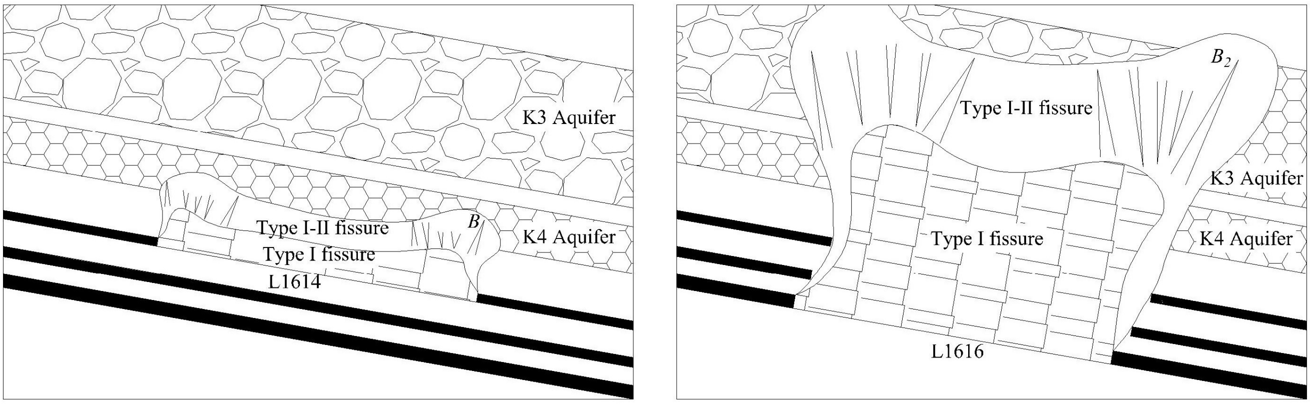

Figure 3. Schematic diagram of the cracking and propagation of the overlying rock fractures.

3.2. Evolutionary Patterns of the Overlying Rock Fractures in the Presence of Water-Resistant Coal Pillars

In compliance with China's Mining Engineering Design Manual, the boundary waterproof coal pillar for a lower coal seam must be established by extending downward from an upper coal-seam's coal pillar boundary, taking into account the mining collapse angle and coal-seam spacing, when the interlayer spacing between the upper and lower coal seams is less than the height of the water-conducting fracture of the lower coal seam post-mining (Figure 4) (Formula (1)) [43].

$$L = l + (H - h) \times (\cot\gamma + \cot\theta), \tag{1}$$

where L denotes the width of the waterproof coal pillar in the lower coal seam, l represents the width of the waterproof coal pillar in the upper coal seam, H is the height of the lower coal-seam water column, h refers to the height of the upper coal-seam water column, γ corresponds to the collapse angle of the uphill rock movement, and θ indicates the collapse angle of the downhill rock movement.

Based on the on-site investigation, the spacing between coal seams #14 and #15 as well as that between #15 and #16 were determined to be 17.3 m and 11.3 m, respectively. The width of the waterproof coal pillar in working face L1813 of coal seam #13 was approximately 20 m, with respective water column heights of 5.8 m, 30.3 m, 50.4 m, and 64.9 m for coal seams #13, #14, #15, and #16. The collapse angle for the uphill and downhill rock movements was approximately 70°. According to Formula (1), the waterproof coal pillar widths for coal seams #14, #15, and #16 were 37.8 m, 52.5 m, and 63 m, respectively. After determining the calculated widths of the waterproof coal pillars for working faces L1814, L1815, and L1816, the three working faces were mined sequentially in a downward direction. A development diagram of the overlying rock fractures is depicted in Figure 5. As the L1814, L1815, and L1816 working faces were successively excavated, the height of the water-conducting fracture increased from 35 m to 103.5 m, spanning between the K3 and K4 aquifers. This fracture only reached up to the K4 aquifer, resulting in minimal water inflow into the three goaf areas.

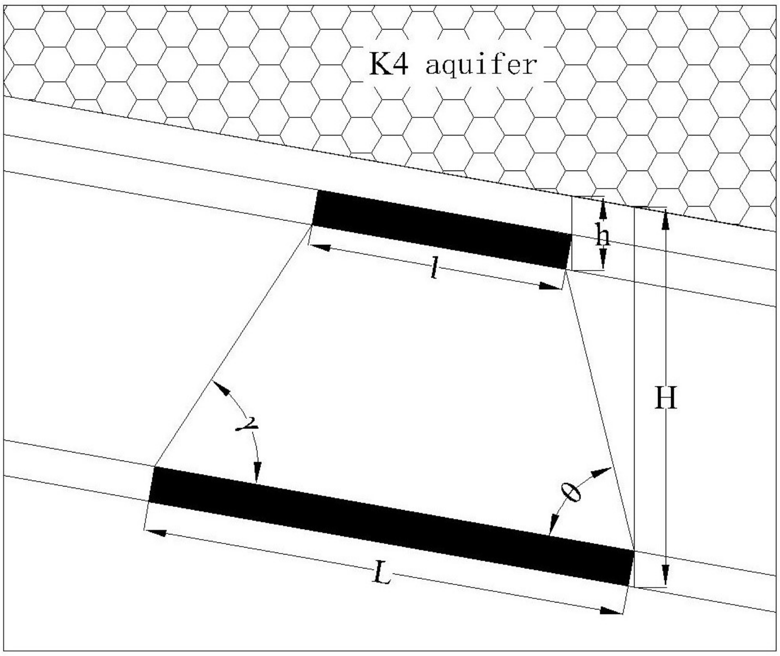

Figure 4. Schematic diagram of waterproof coal pillar retention at the boundaries of adjacent coal-seam mining faces.

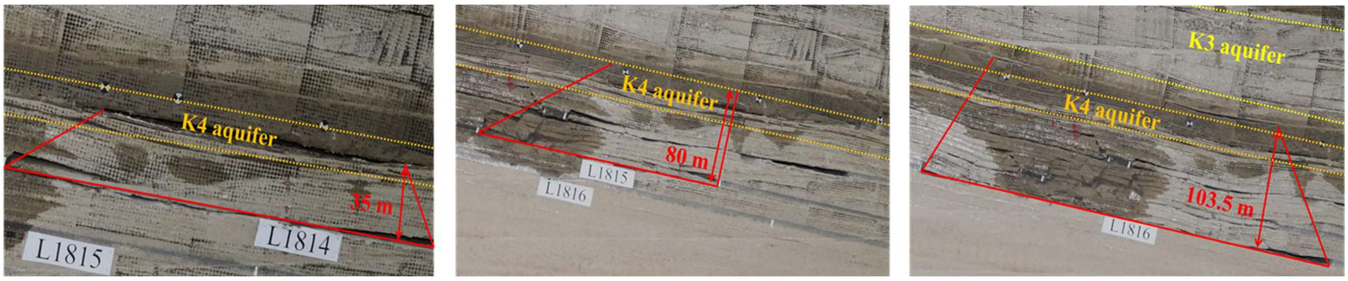

Figure 5. Map illustrating the evolution of the overburden rock fractures in the L1814, L1815, and L1816 working faces post-mining.

3.3. The Dynamics of Sudden Water Inrush in the Working Faces Resulting from Pressure in the K3 Aquifer

Based on an on-site investigation, the K4 and K3 aquifers' initial water pressures were determined to be 3.75 MPa and 37.5 MPa, respectively. The K4 aquifer is close to the #14 coal seam, which suggested that the presence or absence of a waterproof coal pillar in the working face could cause water-conducting fractures to the K4 aquifer. Furthermore, the K3 aquifer's thickness of 87.2 m makes water pressure fluctuation the primary hidden risk factor for water inrush in the working face. To simulate this, water pressure was progressively increased to the K3 aquifer above the L1814, L1815, and L1816 working faces in stages, with increases of 0.1 MPa continuing until the K3 aquifer connected with the lower fracture. The obtained results are presented in Figure 6 and Table 3.

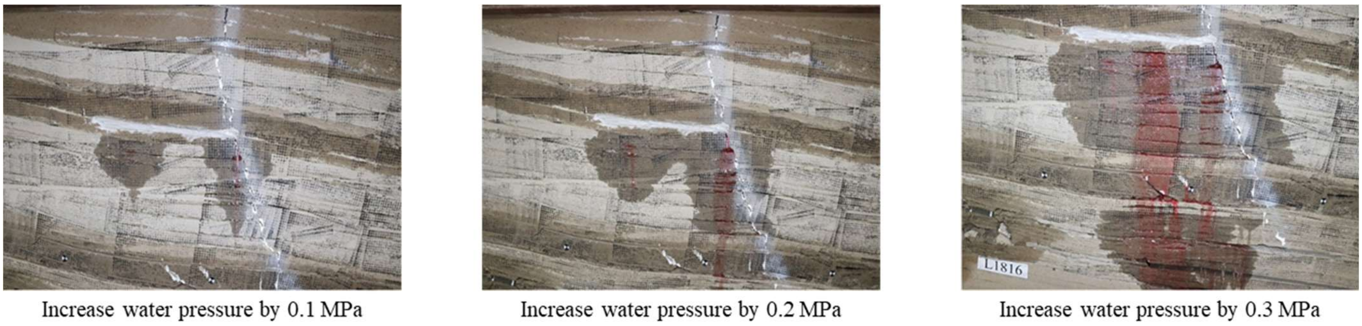
Increase water pressure by 0.1 MPa
Increase water pressure by 0.2 MPa
Increase water pressure by 0.3 MPa

Figure 6. Map illustrating the experimental process of the incremental water pressure increases in the K3 aquifer.

Table 3. Experimental results of the incremental water pressure increases in the K3 aquifer.

Incremental Water Pressure (MPa)	Working Faces	Quantity of Water Inflow Points	Water Inflow Conditions
0.1	L1814 L1815 L1816	1 2 4	Water volumes from the separation layer, vertical fractures, and the central region of the goaf were minimal, with the water inrush volume detected at the monitoring point being 12 mL·s^{-1}.
0.2	L1814 L1815 L1816	3 3 4	Water volumes from the lower separation layer, the central region of the goaf, and the mining stops line were moderate, with the water inrush volume detected at the monitoring point being 33 mL·s^{-1}.
0.3	L1814 L1815 L1816	7 6 6	Water volume from the goaf was significant, with the water inrush volume detected at the monitoring point being 98 mL·s^{-1}.

4. Discussion

The objective of this study was to investigate the mechanisms underlying the anomalous development of water-conducting fractures and the occurrence of water inrush beneath thick sandstone aquifers, taking into account the combined influences of hydraulic fracturing and overlying roof damage. To accomplish this, fracture mechanics principles were utilized to develop a "fracture cracking and propagation model," in tandem with a "hydraulic fracturing-induced disaster model." The 'Fracture Cracking and Propagation Model' was designed to assess the stress state of a particular fracture and deduce its stress intensity factor. This model investigated the direction of fracture cracking and propagation under combined compression–shear loading, incorporating factors such as vertical and horizontal stresses, fracture inclination angles, and stress intensity factors [36–38]. The model offered specific equations for computing these values. Its accuracy was confirmed by juxtaposing its results with simulation tests, thus shedding light on the mechanisms of water-conducting fractures. On the other hand, the 'Hydraulic Fracturing-Induced Disaster Model' delved into the evolution of fractures and water influx beneath sandstone aquifers during hydraulic fracturing operations. This model bifurcated the process into two phases: initially, the pre-existing fractures in the coal-seam roof that ruptured and forged connections with neighboring fractures [39–41], and subsequently, these same fractures after widening, being breached, and causing water inundation from the adjacent aquifers [42]. The key parameters in this model included the compressive–shear stress, the pore water pressure, the fracture inclination angle, the stress intensity factors, and the fracture's energy release rate [43]. Such an approach elucidated the anomalous expansion of water-conducting fractures and water influx beneath expansive sandstone aquifers.

4.1. Fracture Cracking and Propagation Model

4.1.1. Mechanical Model for "Open-Slip" Composite-Type Fractures

The stress analysis was conducted on a specific fracture, designated as fracture A, before establishing a connection between the water-conducting fracture and the K4 aquifer. Fracture A experienced the vertical stress σ_1 and the horizontal stress σ_2. The long axis of fracture A had a length of $2a$, and the angle between the horizontal stress σ_2 and the long axis direction was denoted by α. Figure 7 depicts the stress state of fracture A. Based on the fracture mechanics theory, the stress state of fracture A could be characterized as follows [44]:

$$\begin{cases} \sigma_i = \sigma_1 \cos^2\alpha + \sigma_2 \sin^2\alpha \\ \tau_i = (\sigma_1 - \sigma_2)\sin\alpha\cos\alpha \end{cases}. \tag{2}$$

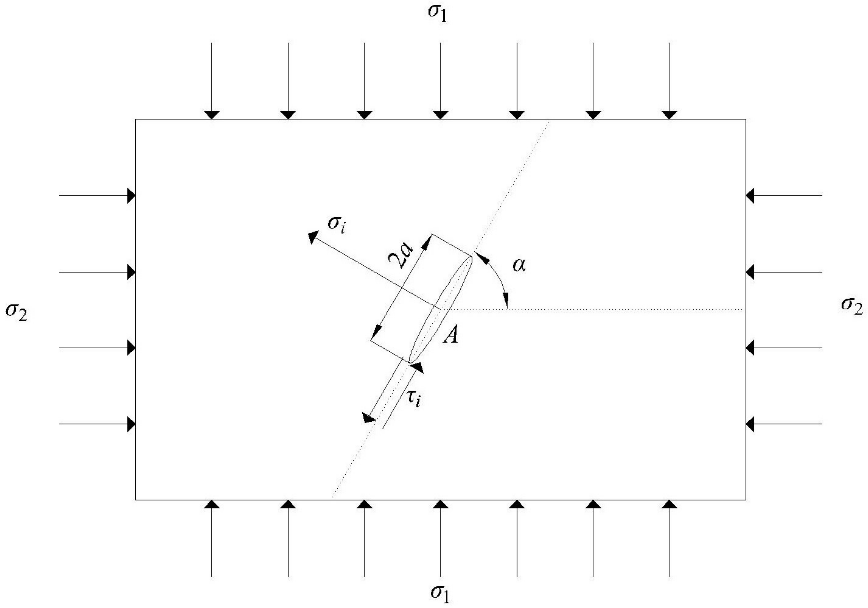

Figure 7. Stress state diagram of Fracture A.

The stress intensity factor for fracture A could be expressed as follows [44]:

$$\begin{cases} K_{\mathrm{I}} = |\sigma_i|\sqrt{\pi a} \\ K_{\mathrm{II}} = |\tau_i|\sqrt{\pi a} \end{cases}, \tag{3}$$

where σ_i represents the normal stress, τ_i denotes the shear stress, α signifies the fracture inclination angle, K_{I} corresponds to the Type I fracture stress intensity factor, K_{II} indicates the Type II fracture stress intensity factor, and a refers to a unit length of 1.

As depicted in Section 3.1, at fracture endpoint B (Figure 3), the vertical stress was -1.31 MPa while the horizontal stress reached -0.69 MPa. The measured shear stress was -0.34 MPa, and the fracture inclination angle stood at 55°. After incorporating these data into Equations (2) and (3), the resulting values were determined as follows: $\sigma_i = -0.89$ MPa, $\tau_i = -0.29$ MPa, $K_{\mathrm{I}} = 1.58$ MPa·m$^{1/2}$, and $K_{\mathrm{II}} = 0.51$ MPa·m$^{1/2}$. The calculated shear stress corresponded with the observed shear stress.

4.1.2. Mechanical Model for Cracking and Propagation of "Open-Slip" Composite-Type Fractures

During the stress analysis of fractures under combined compression–shear loading, the maximum normal stress and maximum shear stress criteria effectively address the cracking angle and provide a solid assessment basis for secondary fractures [45]. As illustrated in Figure 8, a polar coordinate system was established using the tip of fracture A as the coordinate origin. The stress field at the tip of fracture A was represented by a function of the polar coordinates as follows:

$$\begin{cases} \sigma_y = \frac{1}{\sqrt{2\pi r}}\cos\frac{\beta}{2}\begin{bmatrix} K_{\mathrm{I}}\cos^2\frac{\beta}{2}\left(5-4\cos^2\frac{\beta}{2}\right) \\ +\frac{1}{2}K_{\mathrm{II}}\sin\beta\left(4\cos^2\frac{\beta}{2}-3\right) \end{bmatrix} \\ \tau_{xy} = \frac{1}{\sqrt{2\pi r}}\cos\frac{\beta}{2}\begin{bmatrix} \frac{1}{2}K_{\mathrm{I}}\sin\beta\left(4\cos^2\frac{\beta}{2}-3\right) \\ +K_{\mathrm{II}}\left(2-5\cos^2\frac{\beta}{2}+4\cos^4\frac{\beta}{2}\right) \end{bmatrix} \end{cases}, \tag{4}$$

where r denotes the distance between the tips of secondary fracture A_1 and fracture A, measured in unit lengths of 1, and β signifies the polar angle.

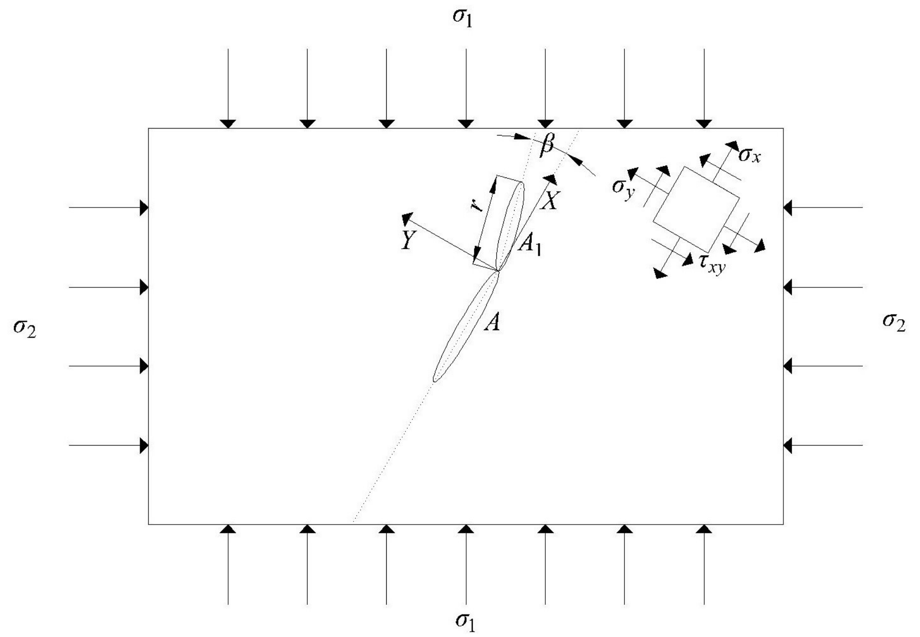

Figure 8. Stress state diagram of Fracture A cracking under a compressive–shear composite load.

As β approached 0° and Formula (4) was applied (with $\beta = \beta_0$), the resulting partial derivative was obtained as follows:

$$\begin{cases} \left(\frac{\partial\sigma_y}{\partial\beta}\right)_{\beta=\beta_0} = -3K_{\mathrm{I}}\cos\frac{\beta_0}{2}\sin\frac{\beta_0}{2} + K_{\mathrm{II}}(\cos^2\frac{\beta_0}{2} - 2\sin^2\frac{\beta_0}{2}) \\ \left(\frac{\partial\tau_{xy}}{\partial\beta}\right)_{\beta=\beta_0} = K_{\mathrm{I}}\cos\frac{\beta_0}{2}(\cos^2\frac{\beta_0}{2} - 2\sin^2\frac{\beta_0}{2}) - K_{\mathrm{II}}\sin\frac{\beta_0}{2} \end{cases}, \tag{5}$$

where β_0 denotes the secondary fracture's cracking angle.

Following the maximum normal stress criterion, setting Equation (5) equal to 0 yielded the following result:

$$-3K_{\mathrm{I}}\cos\frac{\beta_0}{2}\sin\frac{\beta_0}{2} + K_{\mathrm{II}}(\cos^2\frac{\beta_0}{2} - 2\sin^2\frac{\beta_0}{2}) = 0. \tag{6}$$

Similarly, by applying the maximum shear stress criterion and setting Equation (5) equal to 0, the following result was obtained:

$$K_{\mathrm{I}}\cos\frac{\beta_0}{2}(\cos^2\frac{\beta_0}{2} - 2\sin^2\frac{\beta_0}{2}) - K_{\mathrm{II}}\sin\frac{\beta_0}{2} = 0. \tag{7}$$

Upon substituting $K_{\mathrm{I}} = 1.58\ \mathrm{MPa\cdot m^{1/2}}$ and $K_{\mathrm{II}} = 0.51\ \mathrm{MPa\cdot m^{1/2}}$ into Equations (6) and (7), the resulting values for β_0 were found to be 12° and 62°, respectively. With β_0 = 12°, the fracture inclination angle at endpoint B_2 was 67°, which fundamentally concurred with the results of the analogous simulation tests. Conversely, when β_0 was 62°, the fracture inclination angle at endpoint B_2 reached 117°, diverging from the findings of the similar simulation tests. Consequently, the cracking and propagation direction of the fracture closely adhered to the maximum normal stress direction, complying with the maximum normal stress criterion.

4.2. Hydraulic Fracturing-Induced Disaster Model

4.2.1. Mechanical Model for Cracking and Propagation of "Open-Slip" Composite-Type Fractures in Hydraulic Fracturing

Based on the characteristics of the cracking and propagation of mining-induced overburden fractures, the development of these fractures reaching the roof of the K3 aquifer and the subsequent water inrush during close-seam mining beneath the thick sandstone aquifer could be divided into two stages. In the first stage, while mining the L1614 working face, pre-existing fractures in the siltstone roof of the coal seam began to crack and establish connections with adjacent fractures [39–41]. The interconnected fractures subsequently expanded and evolved, extending up to the midpoint of the K4 aquifer. This process was governed by the combined effects of compressive–shear stress and pore water pressure within the aquifer. Water from the K4 aquifer progressively seeped into the goaf through fractures, signifying that cracking and propagation of fracture formations had occurred. In the second stage, as the successive mining of the L1615 and L1616 working faces occurred, the increasingly fractured roof released more energy through the stress–strain field [42,43]. The fractures propagated and widened due to the combined effects of compressive–shear loading and pore water pressure within the aquifer, ultimately breaching the K3 aquifer and extending to its upper boundary. Consequently, water from the K3 aquifer flooded the goaf across an extensive area, signifying that the phase of rapid hydraulic fracturing-induced changes and damage had been reached.

The mechanical model for fracture B under the combined influence of compressive–shear load and pore water pressure could be represented as follows [44]:

$$\begin{cases} \sigma_{i\mathrm{B}} = \sigma_1 \cos^2\alpha + \sigma_2 \sin^2\alpha + P \\ \tau_{i\mathrm{B}} = (\sigma_1 - \sigma_2)\sin\alpha\cos\alpha \\ K_{\mathrm{IB}} = |\sigma_{i\mathrm{B}}|\sqrt{\pi a} \\ K_{\mathrm{IIB}} = |\tau_{i\mathrm{B}}|\sqrt{\pi a} \end{cases}, \tag{8}$$

where P denotes the pore water pressure.

The initial water pressure in the K3 aquifer was −0.1 MPa, whereas the K4 aquifer had an initial water pressure of −0.01 MPa. By substituting $\sigma_1 = -1.31$ MPa, $\sigma_2 = -0.69$ MPa, $\alpha = 55°$, and $P = -0.11$ MPa into Equation (8), the following calculated values were obtained: $\sigma_{i\mathrm{B}} = -1.00$ MPa, $\tau_{i\mathrm{B}} = -0.29$ MPa, $K_{\mathrm{IB}} = 1.77$ MPa·m$^{1/2}$, and $K_{\mathrm{IIB}} = 0.51$ MPa·m$^{1/2}$. Meanwhile, the following results could be obtained by utilizing Equation (4):

$$\begin{cases} \sigma_{y\mathrm{B}} = \frac{1}{\sqrt{2\pi r}}\cos\frac{\beta}{2}\left[K_{\mathrm{IB}}\cos^2\frac{\beta}{2} + \frac{1}{2}K_{\mathrm{IIB}}\sin\beta\right] \\ \tau_{xy\mathrm{B}} = \frac{1}{\sqrt{2\pi r}}\cos\frac{\beta}{2}\left[\frac{1}{2}K_{\mathrm{IB}}\sin\beta + K_{\mathrm{IIB}}\right] \end{cases}. \tag{9}$$

According to the maximum normal stress criterion, the partial derivative of Equation (9) was calculated concerning β, evaluated at $\beta = \beta_1$, and subsequently set to 0, yielding the following result:

$$-3 \times \cos\frac{\beta_1}{2}\sin\frac{\beta_1}{2} + 0.29 \times (\cos^2\frac{\beta_1}{2} - 2\sin^2\frac{\beta_1}{2}) = 0, \tag{10}$$

where β_1 signifies the cracking angles of fractures resulting from the combined influence of compressive–shear stress and pore water pressure.

According to Formula (10), β_1 = 10°. Consequently, the fracture inclination angle at endpoint B_2 was found to be 65°, which corroborated the findings from similar simulation tests.

4.2.2. Mechanical Model for the Extension Heights of "Open-Slip" Composite-Type Fractures in Hydraulic Fracturing

Substituting β_1 = 10° into Equation (9) yielded stress values of $\sigma_{y\mathrm{B}} = -0.71$ MPa and $\tau_{xy\mathrm{B}} = -0.23$ MPa. Utilizing Equation (3), the cracking stress intensity factor for fracture B under the combined influence of compressive–shear stress and pore water pressure could be determined as follows [45]:

$$\begin{cases} K_{\mathrm{IC}} = \left|\sigma_{y\mathrm{B}}\right|\sqrt{\pi \times \frac{r}{2}} \\ K_{\mathrm{IIC}} = \left|\tau_{xy\mathrm{B}}\right|\sqrt{\pi \times \frac{r}{2}} \end{cases}. \tag{11}$$

By substituting $\sigma_{y\mathrm{B}} = -0.71$ MPa, $\tau_{xy\mathrm{B}} = -0.23$ MPa, and $r = 1$ into Equation (11), the following calculated values were obtained: $K_{\mathrm{IC}} = 0.89$ MPa·m$^{1/2}$ and $K_{\mathrm{IIC}} = 0.29$ MPa·m$^{1/2}$.

According to the Griffith criterion [45], the following conclusions could be drawn:

$$G = \frac{{K_{\mathrm{IC}}}^2 + {K_{\mathrm{IIC}}}^2}{E}, \tag{12}$$

where G denotes the energy release rate for fracture B cracking and E represents the elastic modulus of the rock layer in fracture B, with a value of 72.4 MPa.

By substituting $K_{\mathrm{IC}} = 0.89$ MPa·m$^{1/2}$ and $K_{\mathrm{IIC}} = 0.29$ MPa·m$^{1/2}$ into Equation (12), the calculated values yielded $G = 12.1$ MN·m^{-1}.

Similarly, based on the Griffith criterion [45], the variation in the stress intensity factor for fracture B over time could be expressed as follows:

$$\begin{cases} K_{\mathrm{IC}}(t) = \frac{4}{3}\left|\sigma_{y\mathrm{B}}\right|\sqrt{\frac{v_{\mathrm{m}}t\sqrt{1-2v}}{\pi}} \\ K_{\mathrm{IIC}}(t) = \frac{4}{3}\left|\tau_{xy\mathrm{B}}\right|\sqrt{\frac{2v_{\mathrm{m}}t}{\pi}} \end{cases} (t > 0), \tag{13}$$

where v denotes the fracture propagation rate and v_{m} represents the shear wave velocity, with a reference value of 5 m·s^{-1}.

Then, Equations (12) and (13) could be derived simultaneously as follows:

$$\begin{cases} V(t) = 0.48 + \frac{1}{7.76t} - \frac{1}{5.32t^2} \\ S(t) = \int_{120}^{360}(0.48 + \frac{1}{7.76t} - \frac{1}{5.32t^2})d(t) \end{cases} (t > 0) \tag{14}$$

According to Formula (14), the fracture extension height from fracture B to fracture B_2 could be calculated as $S = 115.3$ m. This value was in close agreement with the results obtained from the comparable simulation tests ($S = 125.8$ m). A table of the symbols used in the equations can be found in Nomenclature.

5. Conclusions

(1) The concurrent effects of hydraulic fracturing and damage to the overlying strata are instrumental in the formation of water-conducting fractures and water inrush events beneath thick sandstone aquifers.

(2) The "Fracture Cracking and Propagation Model," grounded in the principles of fracture mechanics, was employed to assess the stress conditions of particular fractures, determining aspects such as stress intensity and the direction of crack propagation.

(3) The "Hydraulic Fracturing-Induced Disaster Model" categorized the evolution of fractures and water inrush into two phases. The initial phase pertained to the fracturing and expansion within the coal-seam roof, whereas the subsequent phase encompassed the broadening and rupturing of fractures, resulting in aquifer-driven inundation.

(4) Detailed computations and formulae were furnished to determine stress values, fracture inclination angles, stress intensity factors, energy release rates, and fracture extension heights. These computational results were juxtaposed against simulation experiments to validate the accuracy of the models.

Author Contributions: Conceptualization, T.Y. and C.Z.; methodology, C.Z.; validation, Q.L. and Q.X.; formal analysis, T.Y.; investigation, T.Y.; resources, C.Z.; data curation, T.Y.; writing—original draft preparation, T.Y.; writing—review and editing, T.Y. and C.Z. All authors have read and agreed to the published version of the manuscript.

Funding: This work was supported by the National Natural Science Foundation of China (grant nos. 52274117 and 51774136) and the Science and Technology Project of Hebei Education Department (grant no. ZC2021103).

Institutional Review Board Statement: Not applicable.

Informed Consent Statement: Not applicable.

Data Availability Statement: The data used to support the findings of this study are available upon request.

Acknowledgments: The authors thank the LingXin Company for their assistance with sampling, and they are indebted to Qingfeng Li and Qian Xu for their help with the partial data analyses.

Conflicts of Interest: The authors declare no conflict of interest. The funders had no role in the design of the study; in the collection, analyses, or interpretation of the data; in the writing of the manuscript; or in the decision to publish the results.

Nomenclature

A table of the symbols used in the equations.

Symbols	**Explanations**
L	The width of the waterproof coal pillar in the lower coal seam
l	The width of the waterproof coal pillar in the upper coal seam
H	The height of the lower coal-seam water column
h	The height of the upper coal-seam water column
γ	The collapse angle of the uphill rock movement
θ	The collapse angle of the downhill rock movement
σ_1	The vertical stress exerted on fracture *A*
σ_2	The horizontal stress exerted on fracture *A*
a	The unit length (equal to 1)
α	The inclination angle of fracture *A*
σ_i	The normal stress exerted on fracture *A*
τ_i	The shear stress exerted on fracture *A*
K_{I}	The Type I fracture stress intensity factor of fracture *A*
K_{II}	The Type II fracture stress intensity factor of fracture *A*
r	The distance between the tips of secondary fracture A_1 and fracture A, measured in unit lengths of 1
β	The polar angle
σ_y	The normal stress exerted on the tip of fracture *A*
τ_{xy}	The shear stress exerted on the tip of fracture *A*
β_0	The cracking angle of fracture *A*
P	The pore water pressure derived from the K3 and K4 aquifers
$\sigma_{i\mathrm{B}}$	The normal stress exerted on fracture *B*
$\tau_{i\mathrm{B}}$	The shear stress exerted on fracture *B*
K_{IB}	The Type I fracture stress intensity factor of fracture *B*
K_{IIB}	The Type II fracture stress intensity factor of fracture *B*
$\sigma_{y\mathrm{B}}$	The normal stress exerted on the tip of fracture *B*
$\tau_{xy\mathrm{B}}$	The shear stress exerted on the tip of fracture *B*
β_1	The cracking angle of fracture *B*

K_{IC}	The Type I cracking stress intensity factor for fracture B
K_{IIC}	The Type II cracking stress intensity factor of fracture B
G	The energy release rate for fracture B cracking
E	The elastic modulus of the rock layer in fracture B
v	The fracture B propagation rate
v_{m}	The shear wave velocity
S	The fracture extension height from fracture B to fracture B_2

References

1. Wu, Q.; Tu, K.; Zeng, Y.F.; Liu, S.Q. Discussion on the main problems and countermeasures for building an upgrade version of main energy (coal) industry in China. *J. China Coal Soc.* **2019**, *44*, 1625–1636.
2. Yin, S.X.; Wang, Y.G.; Li, W.S. Cause, countermeasures and solutions of water hazards in coal mines in China. *Coal. Geol. Explor.* **2023**, *51*, 214–221.
3. Dong, S.N.; Ji, Y.D.; Wang, H.; Zhao, B.F.; Cao, H.D.; Liu, Y.; Liu, Y.F.; Ji, Z.K.; Liu, B.G. Prevention and control technology and application of roof water disaster in Jurassic coal field of Ordos Basin. *J. China Coal Soc.* **2020**, *45*, 2367–2375.
4. Wang, Z.; Li, W.; Hu, Y. Experimental study on mechanical behavior, permeability, and damage characteristics of Jurassic sandstone under varying stress paths. *Bull. Eng. Geol. Environ.* **2021**, *80*, 4423–4439. [CrossRef]
5. Xiong, Y.; Kong, D.; Wen, Z.; Wu, G.; Liu, Q. Analysis of coal face stability of lower coal seam under repeated mining in close coal seams group. *Sci. Rep.* **2022**, *12*, 509. [CrossRef]
6. Pan, W.; Jiang, P.; Li, B.; Li, J.; Yang, Y. The Spatial Evolution Law and Water Inrush Mechanism of Mining-Induced Overburden in Shallow and Short Coal Seam Group. *Sustainability* **2022**, *14*, 5320. [CrossRef]
7. Teng, F.; Yu, M.; Han, X.; Chao, J. Study on the mechanism of coal pillar breaking and fracture development under repeated mining in a close seam group. *Front. Earth Sci.* **2023**, *10*, 991304. [CrossRef]
8. Zhang, P.; Tulu, B.; Sears, M.; Trackemas, J. Geotechnical considerations for concurrent pillar recovery in close-distance multiple seams. *Int. J. Min. Sci. Technol.* **2018**, *28*, 21–27. [CrossRef]
9. Suchowerska, A.M.; Carter, J.P.; Merifield, R.S. Horizontal stress under supercritical longwall panels. *Int. J. Rock Mech. Min. Sci.* **2014**, *70*, 240–251. [CrossRef]
10. Cao, A.; Jing, G.; Dou, L.; Wu, Y.; Zhang, C. Statistical analysis of distribution patterns of coal seams in fold zones in Northwest China. *Int. J. Min. Sci. Technol.* **2018**, *28*, 819–828. [CrossRef]
11. Zhang, J.; Yang, W.; Lin, B.; Zhang, J.; Wang, M. Strata movement and stress evolution when mining two overlapping panels affected by hard stratum. *Int. J. Min. Sci. Technol.* **2019**, *29*, 691–699. [CrossRef]
12. Yang, G.S.; Wang, J.S. Overburden structure evolution and pressure law of second mining in close-range coal seam group. *J. China Coal Soc.* **2018**, *43*, 353–358.
13. Huang, Q.X.; Gao, J. Research on three-field evolution and control effect of pillars structural in shallow buried closely spaced multi-seams mining. *J. China Coal Soc.* **2021**, *12*, 462.
14. Mark, C. An updated empirical model for ground control in US multiseam coal mines. *Int. J. Min. Sci. Technol.* **2021**, *31*, 163–174. [CrossRef]
15. Xie, H.; Gao, M.; Zhang, R.; Peng, G.; Wang, W.; Li, A. Study on the mechanical properties and mechanical response of coal mining at 1000 m or deeper. *Rock Mech. Rock Eng.* **2019**, *52*, 1475–1490. [CrossRef]
16. Liang, Y.; Ran, Q.; Zou, Q.; Zhang, B.; Hong, Y. Experimental study of mechanical behaviors and failure characteristics of coal under true triaxial cyclic loading and unloading and stress rotation. *Nat. Resour. Res.* **2022**, *31*, 971–991. [CrossRef]
17. Yang, B.; Yuan, S.; Zheng, D.; Liu, J.; Kang, J.; Ma, L.; Zhou, Y. Spatial and temporal characteristics of overburden fractures due to repeated mining in close distance coal seams. *J. Min. Saf. Eng.* **2022**, *39*, 255–263.
18. Jia, Q.; Wu, H.; Ling, T.; Liu, K.; Peng, W.; Gao, X.; Zhao, Y. Study on the stress variation law of inclined surrounding rock roadway under the influence of mining. *Minerals* **2022**, *12*, 499. [CrossRef]
19. Bai, E.; Guo, W.; Tan, Y.; Yang, D. The analysis and application of granular backfill material to reduce surface subsidence in China's northwest coal mining area. *PLoS ONE* **2018**, *13*, e0201112. [CrossRef]
20. Li, X.; Ji, D.; Han, P.; Li, Q.; Zhao, H.; He, F. Study of water-conducting fractured zone development law and assessment method in longwall mining of shallow coal seam. *Sci. Rep.* **2022**, *12*, 7994. [CrossRef]
21. Zhu, D.; Tu, S.; Tu, H.; Yang, Z. Mechanisms of support failure and prevention measures under double-layer room mining gobs–a case study: Shigetai coal mine. *Int. J. Min. Sci. Technol.* **2019**, *29*, 955–962. [CrossRef]
22. Zuo, J.; Yu, M.; Li, C.; Sun, Y.; Hu, S.; Li, Z. Analysis of surface cracking and fracture behavior of a single thick main roof based on similar model experiments in western coal mine, China. *Nat. Resour. Res.* **2021**, *30*, 657–680. [CrossRef]
23. Liu, T.; Xu, D.; Shi, L.; Qu, L.; Ji, K. Trapezoidal collapse model to calculate the height of the overburden collapse zone in coal seam mining: An example from Guo'Jiahe Coal Mine, Western China. *Energy* **2022**, *256*, 124609. [CrossRef]
24. Ma, D.; Cai, X.; Li, Q.; Duan, H. In-situ and numerical investigation of groundwater inrush hazard from grouted karst collapse pillar in longwall mining. *Water* **2018**, *10*, 1187. [CrossRef]
25. Zhang, H.; Tu, M.; Cheng, H.; Tang, Y. Breaking mechanism and control technology of sandstone straight roof in thin bedrock stope. *Int. J. Min. Sci. Technol.* **2020**, *30*, 259–263. [CrossRef]

26. Chen, Y.; Zhu, S.; Yang, C.; Xiao, S. Analysis of hydrochemical evolution in main discharge aquifers under mining disturbance and water source identification. *Environ. Sci. Pollut. Res.* **2021**, *28*, 26784–26793. [CrossRef]
27. Yin, H.; Shi, Y.; Niu, H.; Xie, D.; Wei, J.; Lefticariu, L.; Xu, S. A GIS-based model of potential groundwater yield zonation for a sandstone aquifer in the Juye Coalfield, Shangdong, China. *J. Hydrol.* **2018**, *557*, 434–447. [CrossRef]
28. Yu, Z.; Zhu, S.; Wu, Y.; Yu, H. Study on the structural characteristics of the overburden under thick loose layer and thin-bed rock for safety of mining coal seam. *Environ. Earth Sci.* **2020**, *79*, 9. [CrossRef]
29. Guo, J.; Zhang, Q.; Li, Q.; Chen, Z. Study on permeability evolution mechanism of aquifer coal seam roof sandstone under plastic flow. *Geomech. Geophys. Geo-Energy Geo-Resour.* **2021**, *7*, 85. [CrossRef]
30. Li, H.; Chen, Q.; Shu, Z.; Li, L.; Zhang, Y. On prevention and mechanism of bed separation water inrush for thick coal seams: A case study in China. *Environ. Earth Sci.* **2018**, *77*, 759. [CrossRef]
31. Xie, D.; Han, J.; Zhang, H.; Wang, K.; Du, Z.; Miao, T. Risk assessment of water inrush from coal seam roof based on combination weighting-set pair analysis. *Sustainability* **2022**, *14*, 11978. [CrossRef]
32. Gu, D.Z. Theory framework and technological system of coal mine underground reservoir. *J. China Coal Soc.* **2015**, *40*, 239–246.
33. Zhang, T.; Zhao, Y.; Gan, Q.; Nie, X.; Zhu, G.; Hu, Y. Investigations into mining-induced stress–fracture–seepage field coupling in a complex hydrogeology environment: A case study in the Bulianta Colliery. *Mine Water Environ.* **2019**, *38*, 632–642. [CrossRef]
34. Sun, Z.; Bao, W.; Li, M. Comprehensive Water Inrush Risk Assessment Method for Coal Seam Roof. *Sustainability* **2022**, *14*, 10475. [CrossRef]
35. Zhu, L.; Yao, Q.; Xia, Z.; Xu, Q.; Yu, L.; Li, X. Prevention of water and mud inrush in longwall top coal cave mining under shallow buried thin bedrock. *Bull. Eng. Geol. Environ.* **2022**, *81*, 355. [CrossRef]
36. Li, Q.C.; Zhang, C.; Yang, Y.D.; Ansari, U.; Han, Y.; Li, X.Z.; Cheng, Y.F. Preliminary experimental investigation on long-term fracture conductivity for evaluating the feasibility and efficiency of fracturing operation in offshore hydrate-bearing sediments. *Ocean Eng.* **2023**, *281*, 114949. [CrossRef]
37. Li, Q.C.; Han, Y.; Liu, X.; Ansari, U.; Cheng, Y.F.; Yan, C.L. Hydrate as a by-product in CO_2 leakage during the long-term sub-seabed sequestration and its role in preventing further leakage. *Environ. Sci. Pollut. Res.* **2022**, *29*, 77737–77754. [CrossRef]
38. Feng, F.; Chen, S.J.; Wang, Y.J.; Huang, W.P.; Han, Z.Y. Cracking mechanism and strength criteria evaluation of granite affected by intermediate principal stresses subjected to unloading stress state. *Int. J. Rock Mech. Min. Sci.* **2021**, *143*, 104783. [CrossRef]
39. Chen, S.J.; Feng, F.; Wang, Y.J.; Li, D.Y.; Huang, W.P.; Zhao, X.D.; Jiang, N. Tunnel failure in hard rock with multiple weak planes due to excavation unloading of in-situ stress. *J. Cent. South Un.* **2020**, *27*, 2864–2882. [CrossRef]
40. Feng, F.; Chen, S.J.; Han, Z.Y.; Golsanami, N.; Liang, P.; Xie, Z.W. Influence of moisture content and intermediate principal stress on cracking behavior of sandstone subjected to true triaxial unloading conditions. *Eng. Fract. Mech.* **2023**, *284*, 109265. [CrossRef]
41. Zhang, T.; Gan, Q.; Zhao, Y.; Zhu, G.; Nie, X.; Yang, K.; Li, J. Investigations into mining-induced stress–fracture–seepage field coupling effect considering the response of key stratum and composite aquifer. *Rock Mech. Rock Eng.* **2019**, *52*, 4017–4031. [CrossRef]
42. Tian, C.; Wang, A.; Liu, Y.; Jia, T. Study on the migration law of overlying strata of gob-side entry retaining formed by roof cutting and pressure releasing in the shallow seam. *Shock Vib.* **2020**, *2020*, 8821160. [CrossRef]
43. Fang, G.; Liu, Y.; Li, A. Stability evaluation of working face coal pillar in shallow of Shenfu mine district. *Coal Min. Technol.* **2019**, *24*, 56–61. [CrossRef]
44. Wang, Z.Q.; Chen, S.H. *Advanced Fracture Mechanics*; The Press of Science: Beijing, China, 2006.
45. Knott, J.F.; Withey, P.A. *Application Examples of Fracture Mechanics*; The Press of Science: Beijing, China, 1995.